J Mater Sci (2016) 51:2112–2120
DOI 10.1007/s10853-015-9521-z

One-step synthesis of flower-like WO_3/Bi_2WO_6 heterojunction with enhanced visible light photocatalytic activity

Zhenfeng Zhu[1] · Ying Yan[1] · Junqi Li[1]

Received: 27 August 2015 / Accepted: 19 October 2015 / Published online: 26 October 2015

Abstract WO_3/Bi_2WO_6 heterojunctions with flower-like structure were prepared by a facile hydrothermal process without any surfactants or templates. In the heterojunctions, WO_3 nanoparticles were incorporated into three-dimensional flower-like hierarchical Bi_2WO_6. The WO_3/Bi_2WO_6 samples showed much higher photocatalytic activity than pure Bi_2WO_6 did for rhodamine B degradation under visible light irradiation. This could be ascribed to the formation of *n*–*n* type heterojunction, which resulted in the high transfer rate of the photo-generated electron–holes between WO_3 and Bi_2WO_6 and confirmed by photoluminescence and photocurrent measurements.

Introduction

Semiconductor photocatalysts have received much attention due to their abilities of solar energy conversion and environmental purification [1–3]. The semiconductor TiO_2 is considered as one of the best photocatalysts [4, 5]. However, the light response range of TiO_2 is limited to ultraviolet because of the wide band gap (3.2 eV) [6], and the ultraviolet accounts for only about 4 % of entire sunlight [7–9]. So it is significant to prepare new photocatalysts, which can response in large range of sunlight including the visible light which accounts for about 46 % of sunlight.

Bi_2WO_6, an *n*-type semiconductor [10], is exactly a visible-light-driven photocatalyst with a relatively narrow band gap of 2.7 eV [11] ($E_{CB} = 0.24$ eV vs NHE), which has attracted a great deal of attention [12–14]. However, as a single-phase photocatalyst, some drawbacks restrict its further practical application, such as high recombination of the photo-generated electron–hole pairs and low photo quantum efficiency. Fortunately, as preparing a heterojunction is a well-known way to suppress the photo-carriers recombination rate and enhance the photocatalytic property, many materials have been coupled with Bi_2WO_6 to form the heterojunction, such as BiOBr [15], $Bi_2O_2CO_3$ [16], CdS [17], Co_3O_4 [18], WO_3 [19, 20], or $ZnFe_2O_4$ [21]. Among these, WO_3 is an inexpensive and promising material reported to have good photocatalytic performance. As an *n*-type semiconductor with band gap of 2.8 eV ($E_{CB} = 0.74$ eV vs NHE) [22], WO_3 can match well with Bi_2WO_6 to form an *n*–*n* type heterojunction.

Morphology-controlled synthesis of Bi_2WO_6 has been also considered as an efficient way to enhance photocatalytic activities under visible light. Three-dimensional flower-like Bi_2WO_6 photocatalysts have large surface areas and plenty of meso-pores which can effectively harvest visible light due to multiple scattering [23], In addition, the flower-like Bi_2WO_6 structure have been found to increase the active sites and improve the photoenergy conversion efficiency [24]. He et al. [20] have prepared the WO_3 (core)/Bi_2WO_6 (shell) photocatalyst through a hydrothermal reaction and heat treatment. Unfortunately, the preparation process was complex and the advantage of flower-like superstructure Bi_2WO_6 could not survive.

Therefore, for the first time, we successfully prepared the flower-like WO_3/Bi_2WO_6 heterojunction by one-step hydrothermal method without any surfactants or templates. The experimental results show that the flower-like WO_3/Bi_2WO_6 heterojunction has much greater activities for photocatalytic degradation of rhodamine B under visible

✉ Zhenfeng Zhu
zhuzf@sust.edu.cn

[1] School of Materials Science and Engineering, Shaanxi University of Science and Technology, Xi'an 710021, People's Republic of China

light irradiation than pure Bi_2WO_6 does. Moreover, a possible mechanism of WO_3/Bi_2WO_6 on the degradation of RhB is discussed and confirmed by photoluminescence spectra and photocurrent measurements.

Experimental

Preparation of WO_3/Bi_2WO_6

All chemicals are reagent grade and used without further purification. A typical procedure (molar ratio of WO_3/Bi_2WO_6 samples designed as 0.3:1) is as follows: 2 mmol $Bi(NO_3)_3{\cdot}5H_2O$ was firstly dissolved in a 30 mL 0.4 mol/L HNO_3 solution, and then the solution was stirred for 10 min at 40 °C. 30 mL aqueous solution containing 1.3 mmol $Na_2WO_4{\cdot}2H_2O$ was added into the above solution drop by drop and then stirred for 24 h at 40 °C. The obtained white suspension was transferred into a 100-mL Teflon-lined autoclave. The autoclave was heated at 160 °C for 20 h and then cooled to room temperature naturally. The light yellow precipitate was collected and washed with distilled water and ethanol for several times. Then the light yellow precipitate was dried at 60 °C in the air for 10 h. According to this method, WO_3/Bi_2WO_6 samples with different molar ratios of 0.15:1, 0.3:1, and 0.6:1 were also obtained and denoted as 5, 10, and 20 % WO_3/Bi_2WO_6 (mass ratio), respectively. The pure Bi_2WO_6 and WO_3 were also synthesized by a similar procedure.

Characterization

The structure and morphology characterization

The crystal structure of the samples were investigated by X-ray diffraction (XRD, Model No: D/max2200pc, Japan) with Cu K_α radiation ($\lambda = 1.54$ Å) over the range of $10° \leq 2\theta \leq 70°$. The morphology and microstructure of the samples were obtained by field emission scanning electron microscope (FE-SEM, Model No: Hitachi S-4800) and transmission electron microscope (TEM, Model No: FEI Tecnai G2 F20 S-TWIN).

N_2 physisorption analysis

According to the Brunauer–Emmett–Teller analysis (BET, ASAP 2460, Micromeritics, USA), the specific surface areas were determined by nitrogen adsorption–desorption isotherms at 77 K. Prior to measurements, all Bi_2WO_6-based powders were degassed at 473 K for 24 h under a vacuum to ensure a clean, dry surface, free of any loosely bound adsorbed species. The pore size distributions of all samples were calculated from desorption branches of the corresponding nitrogen isotherm by the Barrett–Joyner–Halenda (BJH) method.

Photoluminescence and photoelectrochemical measurements

The photoluminescence measurements were carried out on a Hitachi F-4600 fluorescence spectrophotometer. The photocurrent was conducted by an electrochemical workstation (Model No: CH1660D instruments, shanghai). A three-electrode system was employed using the Ag/AgCl (3 M KCl) electrode as a reference electrode, a Pt wire as the counter electrode and an indium tin oxide (ITO) conducting glass coated with the WO_3/Bi_2WO_6 film as the working electrodes. The WO_3/Bi_2WO_6 film was deposited on ITO glass by the dip-coating method. Briefly, a piece of ITO glass was washed with distilled water and ethanol in an ultrasonic bath for 30 min, and dried at room temperature. In the meantime, WO_3/Bi_2WO_6 (0.02 g) was dispersed in 1 mL distilled water containing 0.5 mL Nafion and ultrasonically treated for 10 min. The as-resulted WO_3/Bi_2WO_6 suspension was deposited onto the surface of ITO using a microsyringe and dried at room temperature. 1 M Na_2SO_4 was used as the electrolyte and a 300 W Xe lamp (wavelength range, distance between sample and lamp) was used as light source. All measurements were carried out at room temperature.

Photocatalytic activity

The photocatalytic activities of the samples were evaluated via the degradation of RhB in an aqueous solution under visible light irradiation. A xenon long-arc lamp GXU 500 with a UV 420-nm cutoff filter was used as the light source to simulate visible light irradiation. In every experiment (seven quartz tubes), 5-mg sample was added into 5 mL RhB aqueous solution with a concentration of 10 mg/L in a quartz tube. Before illumination, the suspensions were sonicated for 30 min and magnetically stirred in the dark for 30 min to reach the adsorption–desorption equilibrium between the photocatalyst and RhB solution. Then the mixture was exposed to the stimulated visible light under magnetic stirring. At given time intervals, 5 mL suspension was taken and centrifuged to remove the photocatalyst. Then the RhB concentration was detected by recording the absorbance at the characteristic band of 553 nm using a Shimadzu UV-2550 UV–vis spectrophotometer.

Results and discussion

Crystal structures

Figure 1 shows XRD patterns of the samples. The pure Bi_2WO_6 is identified as the orthorhombic Bi_2WO_6 (JCPDS

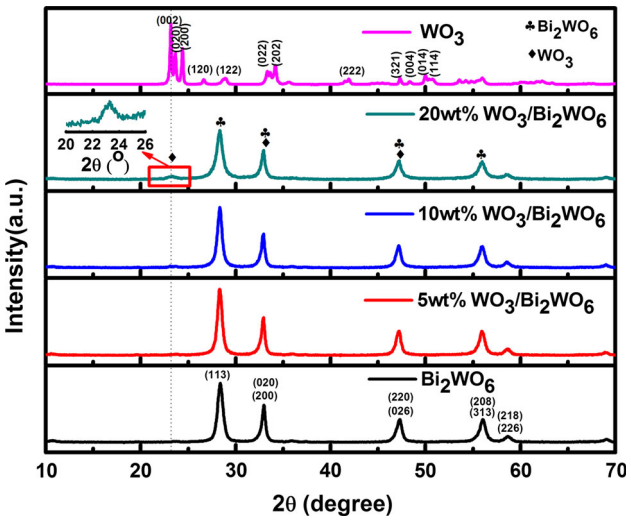

Fig. 1 XRD patterns of WO_3, Bi_2WO_6, and WO_3/Bi_2WO_6 samples. The *inset* is partial magnification of XRD pattern of 20 % WO_3/Bi_2WO_6 sample

NO. 39-0256) without any impurity. The pure WO_3 is identified as monoclinic WO_3 (JCPDS NO. 72-1465) without any impurity. For the WO_3/Bi_2WO_6 samples, XRD patterns consist of Bi_2WO_6 and WO_3 diffraction peaks. As shown in the inserted figure for the 20 % WO_3/Bi_2WO_6 sample, the diffraction peaks of WO_3 can be observed. The strongest peak of WO_3 is attributed to (002) plane, which is in good agreement with the following HRTEM analyses. No impurity peak is also found in the WO_3/Bi_2WO_6 heterojunction. This suggests that the photocatalyst is only composed of orthorhombic Bi_2WO_6 and monoclinic WO_3.

Figure 1 shows XRD patterns of the samples. The pure Bi_2WO_6 is identified as orthorhombic Bi_2WO_6 (JCPDS NO. 39-0256) without any impurity. The pure WO_3 is identified as monoclinic WO_3 (JCPDS NO. 72-1465) without any impurity. For the WO_3/Bi_2WO_6 samples, XRD patterns consist of Bi_2WO_6 and WO_3 diffraction peaks. As shown in the inserted figure for the 20 % WO_3/Bi_2WO_6 sample, the diffraction peaks of WO_3 can be observed. The strongest peak of WO_3 is attributed to (002) plane, which is in good agreement with the following HRTEM analyses. No impurity peak is also found in the WO_3/Bi_2WO_6 heterojunction. This suggests that the photocatalyst is only composed of orthorhombic Bi_2WO_6 and monoclinic WO_3.

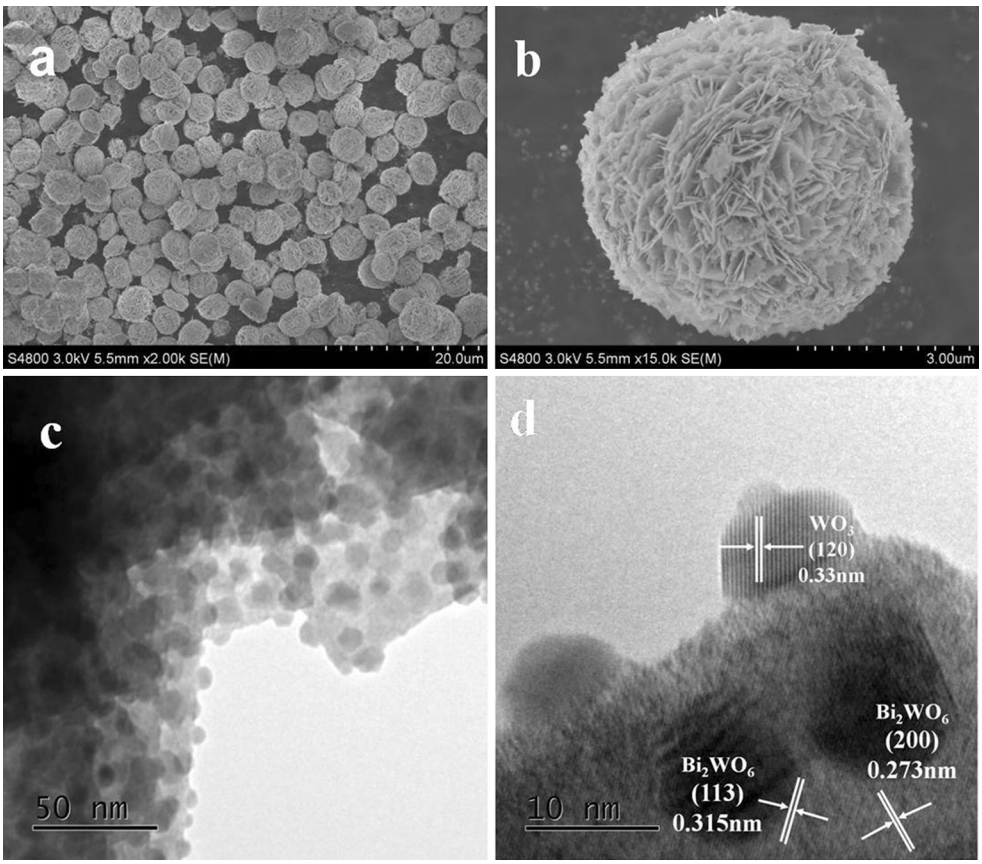

Fig. 2 SEM images of **a** overall morphology and **b** a detailed view on an individual sphere, **c** TEM and **d** HRTEM images of the 5 % WO_3/Bi_2WO_6

Morphology characterization

The morphology and microstructure of the 5 % WO_3/Bi_2WO_6 sample were investigated by SEM and TEM. Figure 2a shows that the 5 % WO_3/Bi_2WO_6 sample consists of spherical particles with diameter ranging from 3 to 5 μm. All the spherical particles are well dispersed. Figure 2b is image with high magnification of an individual 5 % WO_3/Bi_2WO_6 spherical particle which reveals more detailed structural characteristics of the heterojunction photocatalysts. We can see that the spherical particle is flower-like and consists of two-dimensional thin nanoplates with many different pores, which can serve as transport paths for small molecules and then improve the photocatalytic property. More in-depth information of the sample can be observed by TEM (Fig. 2c) and HRTEM micrographs (Fig. 2d). There are many nanoparticles with the diameter about 10 nm attached to the nanoplate. By carefully measuring the lattice parameters with Digital Micrograph and comparing with the data in JCPDS, three different kinds of lattice fringes with spacing of 0.273, 0.315, and 0.33 nm are obtained. It can be sure that the lattice fringes with spacing of 0.273 and 0.315 nm belong to the (200) and (113) crystallographic plane of orthorhombic Bi_2WO_6 (JCPDS NO. 39-0256) and the lattice fringe with spacing of 0.33 nm belongs to (120) plane of monoclinic WO_3 (JCPDS NO. 72-1465). So the nanoplates could be Bi_2WO_6 and the nanoparticles on the surface of the nanoplates could be WO_3.

Figure 3 is SEM micrograph of all the samples: (a) pure Bi_2WO_6; (b) 5 % WO_3/Bi_2WO_6; (c) 10 % WO_3/Bi_2WO_6; and (d) 20 % WO_3/Bi_2WO_6. All the samples exhibit flower-like structure which consists of nanoplates. From the inserted figures, we can see that with increasing WO_3 doping content, the nanoplates become denser and thinner, at the same time, the pores among the nanoplates become smaller and smaller. The thickness of the nanoplates is about 27, 20, 17, and 12 nm for the WO_3 content of 0, 5, 10, and 20 %, respectively.

N_2 physisorption analysis

The analysis of surface area and pore size are carried out to establish correlations, which derived from the nitrogen molecules that are physisorbed by these composite photocatalysts [25]. The nitrogen adsorption/desorption isotherms and the corresponding BJH pore size distribution curves of the pure Bi_2WO_6 and 5 % WO_3/Bi_2WO_6 composite are shown in Fig. 4. It can be seen that the pure Bi_2WO_6 and 5 % WO_3/Bi_2WO_6 heterojunction exhibit the typical type-III curves for mesoporous materials according to IUPAC classification (Fig. 4a). The specific surface areas are calculated using the BET method and the pore size distribution of the each sample is calculated from the

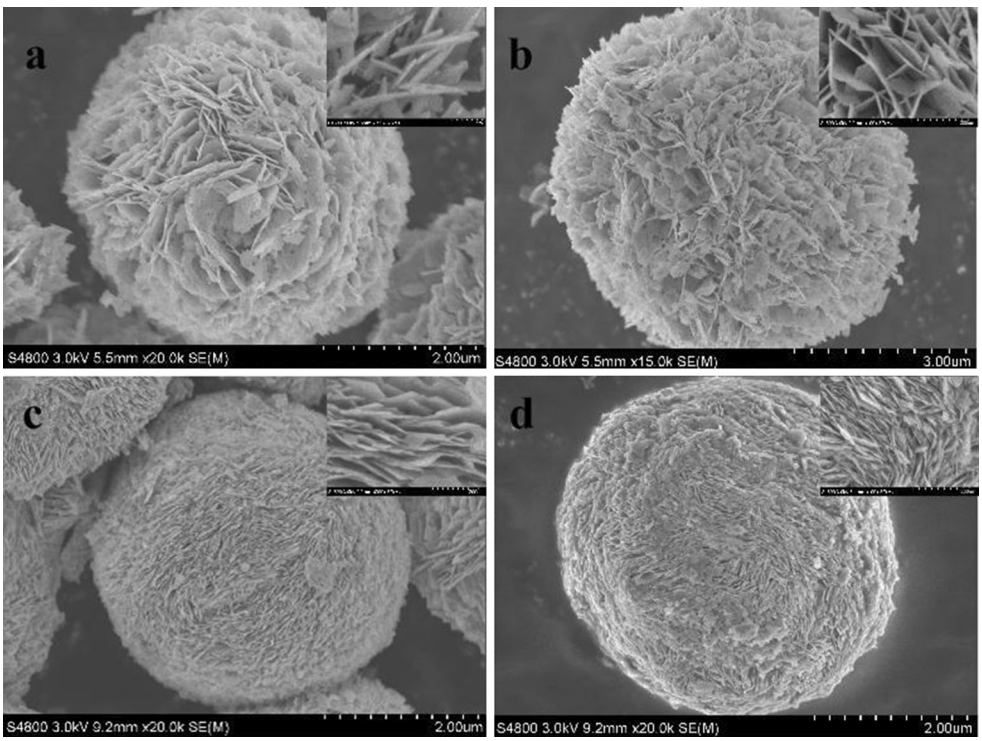

Fig. 3 SEM micrographs of the samples: **a** pure Bi_2WO_6; **b** 5 % WO_3/Bi_2WO_6; **c** 10 % WO_3/Bi_2WO_6; and **d** 20 % WO_3/Bi_2WO_6

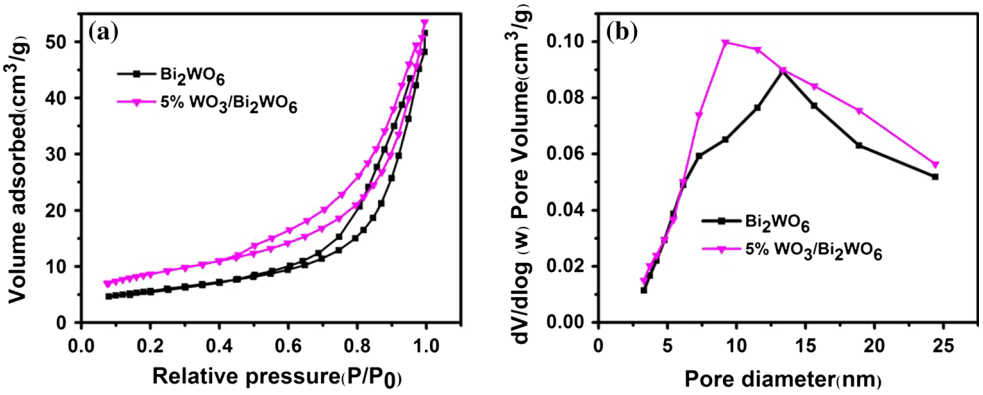

Fig. 4 **a** Nitrogen adsorption/desorption isotherm curves; **b** BJH pore size distribution curves of pure Bi_2WO_6 and 5 % WO_3/Bi_2WO_6 samples

Table 1 Adsorption parameters and the pseudo-first-order kinetic (k) value of Bi_2WO_6 and all WO_3/Bi_2WO_6 samples

Sample	BET surface area (m^2/g)	Pore size (nm)	K (min^{-1})
Bi_2WO_6	17.41	13.92	0.006
5 % WO_3/Bi_2WO_6	26.01	9.73	0.012
10 % WO_3/Bi_2WO_6	30.18	8.59	0.030
20 % WO_3/Bi_2WO_6	45.75	6.42	0.018

desorption branch of the isotherms using the BJH algorithm (Fig. 4b). As seen in Table 1, with increasing the content of WO_3, the BET specific surface area becomes larger and larger and the BJH pore size becomes smaller and smaller.

Photoluminescence spectra analysis

PL spectrum is useful to reveal the migration, transfer, and recombination process of the photo-generated electron–hole pairs in the semiconductor. In order to demonstrate the separated efficiency of the electron–hole pairs, the room temperature photoluminescence (PL) spectra were examined for Bi_2WO_6 and all WO_3/Bi_2WO_6 samples with an excitation wavelength of 300 nm. As shown in Fig. 5, all samples show an apparent characteristic emission peak from 400 to 500 nm. The strongest emitting peak at 455 nm can be attributed to the radiative recombination process of self-trapped excitations [26]. Compared with pure Bi_2WO_6, all WO_3/Bi_2WO_6 samples have a weaker PL intensity and the 5 % WO_3/Bi_2WO_6 sample shows the lowest emission peak. A weaker intensity of the peak represents a lower recombination probability of free charges. So couple WO_3 with Bi_2WO_6 has improved the separated efficiency of the electron–hole pairs and the 5 % WO_3/Bi_2WO_6 sample has the best performance.

Transient photocurrent analysis

We also have measured transient photocurrent to gain an insight into the high separation efficiency of the photo-generated electrons and holes in the Bi_2WO_6 and WO_3/Bi_2WO_6 samples. Figure 6 displays the photocurrent–time

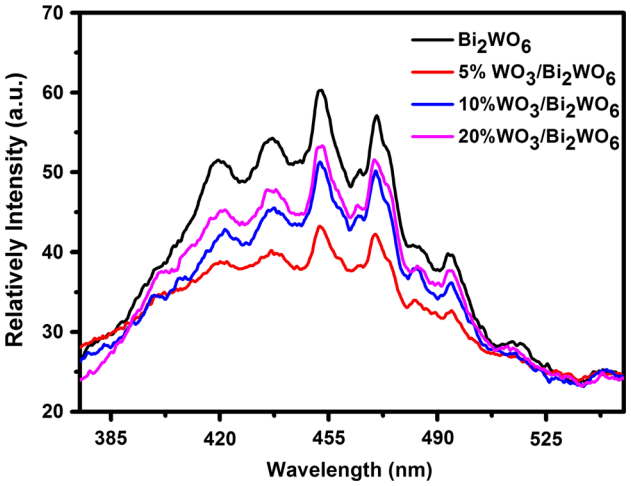

Fig. 5 Photoluminescence (PL) spectra of Bi_2WO_6 and WO_3/Bi_2WO_6 samples

(I–t) curves of the four samples with typical on–off cycles of intermittent visible light irradiation. As shown in Fig. 6, the photocurrent boosts rapidly once the light is turned on and returns quickly to its dark current state when the light is turned off. The initial current is due to the separation of the electron–hole pairs at the semiconductor/electrolyte interface: holes are trapped by the reduced species in the electrolyte, while electrons transport to the back contact substrate [27]. As WO_3 concentration increases, the photocurrent increases until WO_3 doping content is 5 % and then decreases. This dependence corresponds well to the above PL results.

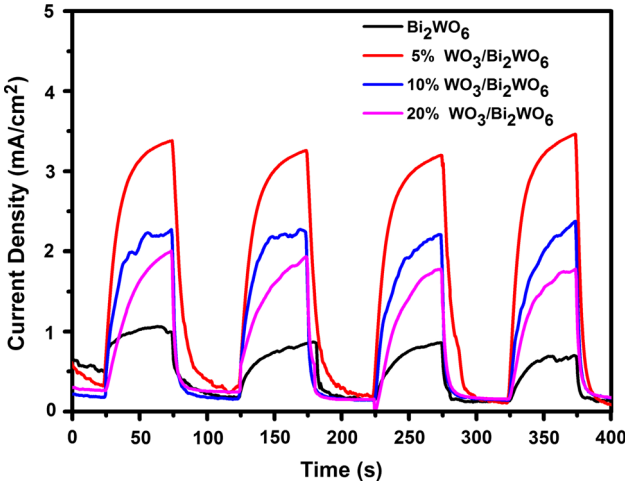

Fig. 6 Photocurrent transient responses for Bi_2WO_6 and WO_3/Bi_2WO_6 samples

Photocatalytic activity

Figure 7a shows the photocatalytic degradation efficiency of RhB in the presence of different samples under visible light irradiation. The blank test confirms that the photocatalytic degradation of RhB can be ignored without catalyst. All heterojunctions show higher photocatalytic activity than pure Bi_2WO_6 dose and the 5 % WO_3/Bi_2WO_6 shows the highest photocatalytic activity. It can be observed that only 48.9 and 32.1 % RhB is photodegraded by pure Bi_2WO_6 and WO_3 under visible light in 100 min, respectively. 5 % WO_3/Bi_2WO_6 can result in 98.5 % degradation rate in the same condition. However, to further increase the amount of WO_3, photocatalytic activity of RhB is decreased to 93 % in the same condition. According to the above SEM, BET specific surface areas and BJH pore size distribution results, we think that the suitable amount of WO_3 can uniformly distribute on the surface of flower-like Bi_2WO_6 and make the nanoplates become density and thin which is helpful to improve the photocatalytic activity. However, the excess WO_3 makes flower-like Bi_2WO_6 overlap and agglomerate which prevent the transport paths for organic molecules and then lower photocatalytic property. The results indicate that the suitable content of WO_3 plays an important role in the enhancement of photocatalytic performance.

For a better comprehension of the photocatalytic activity of catalysts, the reaction kinetic of the RhB degradation was investigated. The experimental data were fitted by the relevant equation as below: $-\ln(C/C_0) = kt$, where C_0 and C are the concentrations of RhB at adsorption–desorption equilibrium and the reaction time t, respectively, and k is the apparent first-order rate constant. As shown in Fig. 7b, upon varying the WO_3 content within 5.0–20 %, the plots of the (C_0/C) versus irradiation time (t) display a nearly straight line. All WO_3/Bi_2WO_6 heterojunctions show higher photodegraded efficiency than pure Bi_2WO_6 and WO_3 do. The 5 % WO_3/Bi_2WO_6 exhibits the highest photodegraded efficiency and is about fivefold compared to that of the pure Bi_2WO_6 sample (Table 1).

In order to demonstrate the photocatalytic activities of WO_3/Bi_2WO_6 samples with WO_3 mass ratio between 0 and 5 %, we do experiment about 3 % WO_3/Bi_2WO_6 sample. As is shown in Fig. 8, all strong peaks can be ascribed to the orthorhombic Bi_2WO_6 (JCPDS NO. 39-0256). No clear diffraction peak belonging to WO_3 is observed, due to the small amount of WO_3 and their highly dispersion in WO_3/Bi_2WO_6 sample (Fig. 8a). It can be observed that the flower-like superstructure cannot be destroyed and also consist of two-dimensional nanoplates (Fig. 8b). The specific surface areas and pore size distribution is 23.68 m^2/g and 11.37 nm, respectively (Fig. 8c). The photocatalytic activity indicates that the 3 % WO_3/Bi_2WO_6 heterojunction exhibits lower photocatalytic activity (90.2 % RhB be photodegraded) than 5 % WO_3/Bi_2WO_6 does due to the small amount of WO_3 loading (Fig. 8d).

Circulation experiment

Figure 9a shows the variations of the UV–vis absorption spectra of RhB solutions in the presence of 5 % WO_3/

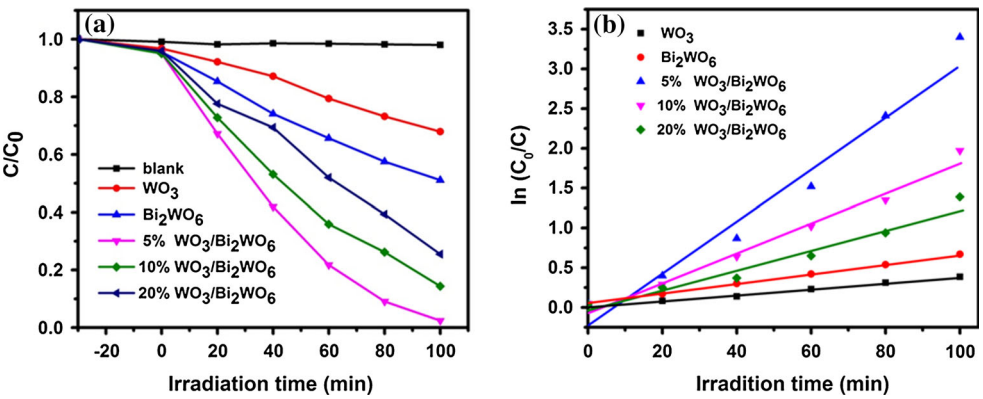

Fig. 7 **a** Photocatalytic degradation curve and **b** first-order plots for the photodegradation of RhB in the presence of WO_3, Bi_2WO_6, and WO_3/Bi_2WO_6 samples under visible light irradiation

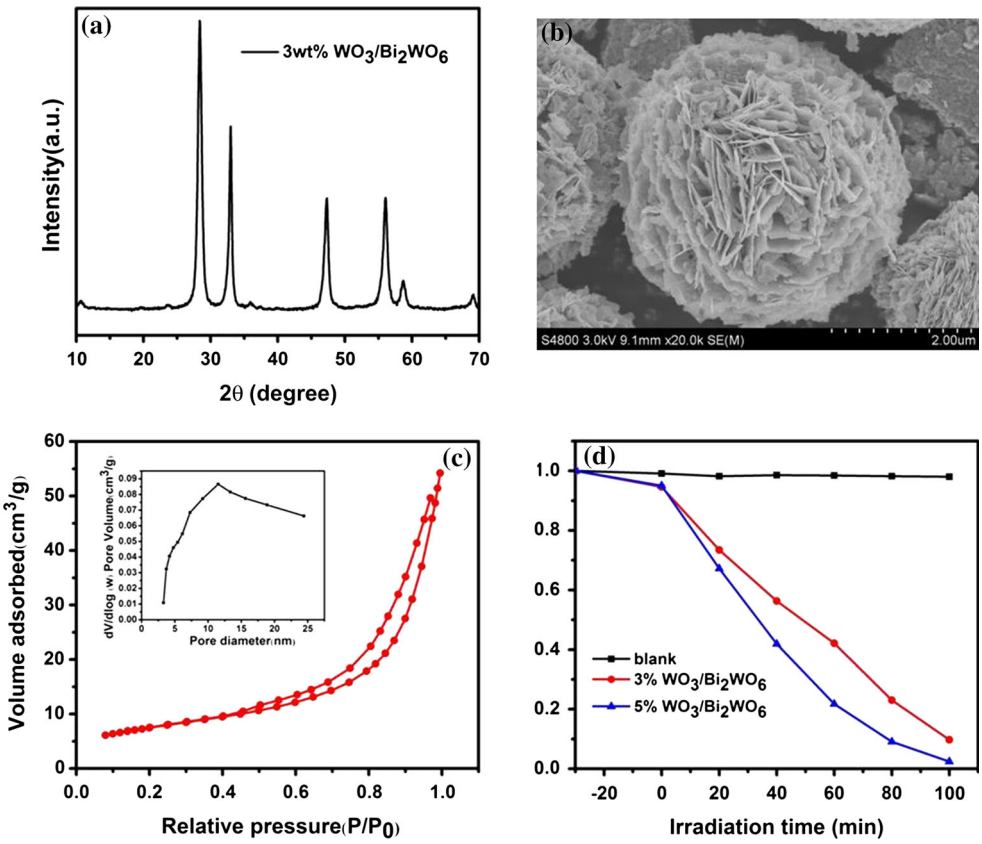

Fig. 8 **a** XRD pattern, **b** SEM micrograph, **c** nitrogen adsorption/desorption isotherm curve and BJH pore size distribution curve, **d** photocatalytic degradation curve of 3 % WO_3/Bi_2WO_6 sample

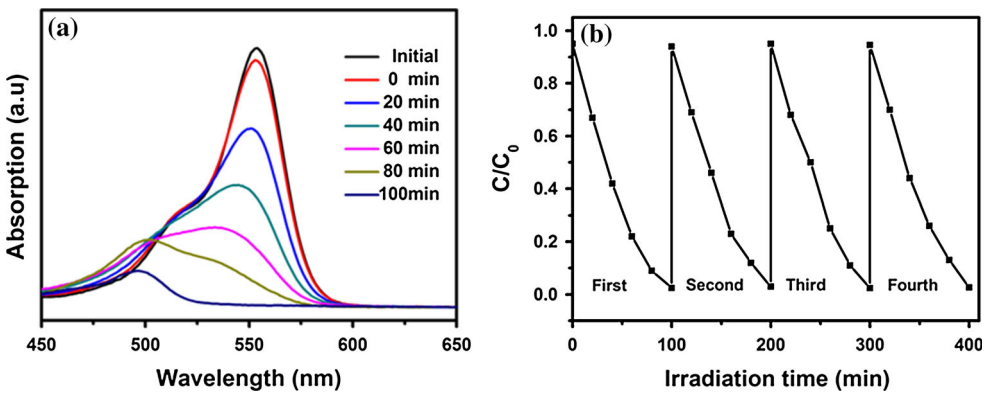

Fig. 9 **a** The UV–vis absorption spectra and **b** cycling runs for the degradation of RhB in the presence of 5 % WO_3/Bi_2WO_6 under visible light irradiation

Bi_2WO_6 heterojunction under visible light irradiation ($\lambda > 420$ nm), which shows a maximum absorption band at 553 nm. With the increase of irradiation time, a rapid decrease of RhB absorption band is observed and the color of the suspension gradually changes from pink to light green. In addition, the maximum absorption peak of RhB gradually shifts to blue region, which can be attributed to a successive de-ethylation from the aromatic rings and destruction of the conjugated structure process, according to the formation of the different de-ethylated rhodamine intermediates [28]. To evaluate the stability of 5 % WO_3/Bi_2WO_6, the circulating runs in the photodegradation of RhB under visible light were checked. As shown in Fig. 9b, after every 100 min of photodegradation, the separated photocatalysts were washed with deionized water and dried to remove the ions absorbing on its surface after every reaction. There is no obvious catalyst deactivation after four cycling runs and the flower-like structure do not change. The reasons for this little decrease may be some catalysts washout during the repetitive steps. The results indicate that the *n–n* type photocatalyst exhibits excellent stability, reusability, and less photocorrosion during the photocatalytic reaction.

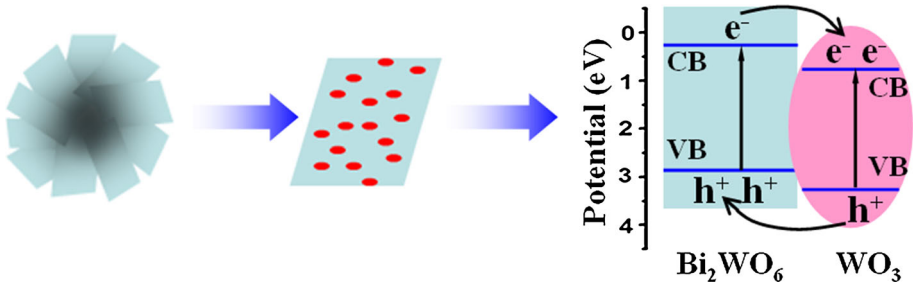

Fig. 10 Photocatalytic mechanism of WO_3/Bi_2WO_6 samples

The role of WO_3

About the influence of WO_3 concentration on the photocatalytic activity, two effects should be considered: on one hand, WO_3 concentration affects morphology of the sample (as shown in Fig. 3). As WO_3 concentration increases, the nanoplates become denser and thinner and the pores among the nanoplates become smaller and smaller. This may be helpful to increase the specific surface area and the active sites in porous microsphere. On the other hand, WO_3 concentration affects photo-carriers recombination rate of the sample (as shown in Figs. 5, 6). The addition of WO_3 has suppressed photo-carriers recombination due to the formation of *n–n* type heterojunction, which is helpful to improve the sample photocatalytic activity. However, the suppression effect of heterojunction does not monotonically increase with the WO_3 concentration increasing. From Figs. 5 and 6, we can see that 5 % WO_3/Bi_2WO_6 exhibits the highest separated efficiency of the photo-carriers. In above two respects, the latter effect is expected to dominate. So the sample photocatalytic activities show the dependence on WO_3 concentration: as WO_3 concentration increases, the photocatalytic activities increase until WO_3 mass ratio is 5 % and then decreases.

Photocatalytic mechanism

To better understand the photocatalytic mechanism of the *n–n* type WO_3/Bi_2WO_6 heterojunction, a possible mechanism on the degradation of RhB is shown in Fig. 10. The optical band gap energy of Bi_2WO_6 and WO_3 is 2.7 eV ($E_{CB} = 0.24$ vs NHE) and 2.8 eV ($E_{CB} = 0.74$ eV vs NHE), respectively. The band gaps of the two semiconductors match well with each other. Under visible light irradiation, both the Bi_2WO_6 and WO_3 are excited by absorbing photons, and then electron–hole pairs are produced. The WO_3 acts as electron-accepting semiconductor. Photo-generated electrons transfer from the conduction band (CB) of Bi_2WO_6 to that of WO_3. Simultaneously, holes shift from the valence band (VB) of WO_3 to that of Bi_2WO_6. The effectively separation of photo-generated electrons and holes can be enhanced, which result in higher photocatalytic performance.

Conclusions

In summary, the flower-like WO_3/Bi_2WO_6 heterojunction with different WO_3 concentrations was prepared via the one-step hydrothermal method. The flower-like superstructure is composed of Bi_2WO_6 nanoplates and WO_3 nanoparticles. The WO_3 concentration has a great influence on the morphology and photocatalytic activity of WO_3/Bi_2WO_6 heterojunction. As WO_3 concentration increases, the nanoplates become denser and thinner, and the photocatalytic activities increase until mass ratio of WO_3 is up to 5 % and then decreases. The result indicates that *n–n* type heterojunction has better photocatalytic activity than pure Bi_2WO_6 does, because electrons can be injected from the CB of Bi_2WO_6 to that of WO_3 under visible irradiation. Thus, the photo-generated electrons and holes are efficiently separated at the intimate interface of heterojunction in time. Therefore, the flower-like WO_3/Bi_2WO_6 heterojunction has good potential for application to organic pollutants purification.

Acknowledgements We acknowledge financial support from the National Science Foundation of China (51272147), the Academic Backbone Cultivation Program of Shaanxi University of Science & Technology (XSGP201203), and the Graduate Innovation Fund of Shaanxi University of Science and Technology.

References

1. Chen CC, Ma WH, Zhao JC (2010) Semiconductor-mediated photodegradation of pollutants under visible-light irradiation. Chem Soc Rev 39:4206–4219
2. Hoffmann M, Martin S, Choi WY, Bahnemannt D (1995) Environmental applications of semiconductor photocatalysis. Chem Rev 95:69–96
3. Hagfeldt A, Gratzel M (1995) Light-induced redox reactions in nanocrystalline systems. Chem Rev 95:49–68
4. Ge L, Han CC, Liu J (2011) Novel visible light-induced g-C_3N_4/Bi_2WO_6 composite photocatalysts for efficient degradation of methyl orange. Appl Catal B 108:100–107
5. Li JQ, Liu ZX, Wang DF, Zhu ZF (2014) Visible-light responsive carbon-anatase-hematite core-shell microspheres for methylene blue photodegradation. Mater Sci Semicond Process 27:950–957
6. Wu L, Yu JC, Wang XC, Zhang LZ, Yu JG (2005) Characterization of mesoporous nanocrystalline TiO_2 photocatalysts synthesized via a sol-solvothermal process at a low temperature. J Solid State Chem 178:321–328

7. Zhang L, Zhu YF, He Y, Li W, Sun HB (2003) Preparation and performances of mesoporous TiO_2 film photocatalyst supported on stainless steel. Appl Catal B 40:287–292
8. Ge L, Xu MX, Fang HB (2006) Photo-catalytic degradation of methyl orange and formaldehyde by Ag/$InVO_4$-TiO_2 thin films under visible-light irradiation. J Mol Catal A Chem 258:68–76
9. Li JQ, Wang DF, Guo ZY, Zhu ZF (2012) Preparation, characterization and visible-light-driven photocatalytic activity of Fe-incorporated TiO_2 microspheres photocatalysts. Appl Surf Sci 263:382–388
10. Li ZQ, Chen XT, Xue ZL (2013) Microwave-assisted synthesis and photocatalytic properties of flower-like Bi_2WO_6 and Bi_2O_3–Bi_2WO_6 composite. J Colloid Interface Sci 394:69–77
11. Ge L, Liu J (2011) Efficient visible light-induced photocatalytic degradation of methyl orange by QDs sensitized CdS-Bi_2WO_6. Appl Catal B 105:289–297
12. Zhang ZJ, Wang WZ, Yin WZ, Shang M, Wang L, Sun SM (2010) Inducing photocatalysis by visible light beyond the absorption edge: effect of up conversion agent on the photocatalytic activity of Bi_2WO_6. Appl Catal B 101:68–73
13. Wang XJ, Chang LL, Wang JR, Song NN, Liu HL, Wan XL (2013) Facile hydrothermal synthesis of Bi_2WO_6 microdiscs with enhanced photocatalytic activity. Appl Surf Sci 270:685–689
14. Zhang N, Ciriminna R, Pagliaro M, Xu YJ (2014) Nanochemistry-derived Bi_2WO_6 nanostructures: towards production of sustainable chemicals and fuels induced by visible light. Chem Soc Rev 43:5276–5287
15. Xia JX, Di J, Yin S, Xu H, Zhang J, Xu YG, Xu L, Li HM, Ji MX (2014) Facile fabrication of the visible-light-driven Bi_2WO_6/BiOBr composite with enhanced photocatalytic activity. RSC Adv 4:82–90
16. Huang XW, Chen HF (2013) One-pot hydrothermal synthesis of $Bi_2O_2CO_3$/Bi_2WO_6 visible light photocatalyst with enhanced photocatalytic activity. Appl Surf Sci 284:843–848
17. Ge L, Liu J (2011) Synthesis and photocatalytic performance of novel CdS quantum dots sensitized Bi_2WO_6 photocatalysts. Mater Lett 65:1828–1831
18. Xiao Q, Zhang J, Xiao C, Tan XK (2008) Photocatalytic degradation of methylene blue over Co_3O_4/Bi_2WO_6 composite under visible light irradiation. Catal Commun 9:1247–1253
19. Gui MS, Zhang WD (2012) One-step hydrothermal preparation strategy for nanostructured WO_3/Bi_2WO_6 heterojunction with high visible light photocatalytic activity. Chem Eng J 197:283–288
20. He GH, He GL (2014) Synthesis and visible light photocatalytic behavior of WO_3 (core)/Bi_2WO_6 (shell). J Mol Catal A Chem 385:106–111
21. Li JQ, Liu ZX, Zhu ZF (2014) Magnetically separable ternary hybrid of $ZnFe_2O_4$-Fe_2O_3-Bi_2WO_6 hollow nanospheres with enhanced visible photocatalytic property. Appl Surf Sci 320:146–153
22. Chen SF, Hu YF, Meng SG, Fu XL (2014) Study on the separation mechanisms of photogenerated electrons and holes for composite photocatalysts g-C_3N_4-WO_3. Appl Catal B 150–151:564–573
23. Li XN, Huang RK, Hu YH, Chen YJ, Liu WJ, Yuan RS, Li ZH (2012) A templated method to Bi_2WO_6 hollow microspheres and their conversion to double-shell Bi_2O_3/Bi_2WO_6 hollow microspheres with improved photocatalytic performance. Inorg Chem 51:6245–6250
24. Li JQ, Guo ZY, Zhu ZF (2012) Ag/Bi_2WO_6 plasmonic composites with enhanced visible photocatalytic activity. Ceram Int 40:6495–6501
25. Kibombo HS, Rasalingam S, Koodali RT (2013) Facile template free method for textural property modulation that enhances adsorption and photocatalytic activity of aperiodic titania supported silica materials. Appl Catal B 142–143:119–128
26. Huang HW, Wang SB, Tian N, Zhang YH (2014) A one-step hydrothermal preparation strategy for layered $BiIO_4$/Bi_2WO_6 heterojunctions with enhanced visible light photocatalytic activities. RSC Adv 4:5561–5567
27. Tian BZ, Dong RF, Zhang JM, Bao SY, Yang F, Zhang JL (2014) Sandwich-structured AgCl@Ag@TiO_2 with excellent visible-light photocatalytic activity for organic pollutant degradation and *E. coli* K12 inactivation. Appl Catal B 158–159:76–84
28. Cruz AM, Ctrica UM, León UAN, Universitaria C (2010) Photocatalytic properties of $BiVO_4$ prepared by the co-precipitation method: degradation of rhodamine B and possible reaction mechanisms under visible irradiation. Mater Res Bull 45:135–141